# CHAPTER 4

# RESULTS AND DISCUSSION (PART I): PREPARATION AND CHARACTERISTICS OF BNZ SYSTEM

In this chapter, the fabrication and characterization of $Bi_{0.5}Na_{0.5}ZrO_3$ (BNZ) system are examined and discussed. Powder processing and phase formation are focused initially. The crystal structure determination of BNZ powder is subsequently performed. Finally, BNZ ceramic fabrication with different processing factors is investigated in order to obtain a dense sample.

## 4.1 BNZ powder preparation

As a novel perovskite material synthesis, Goldschmidt tolerance factor ($t$) should be mentioned first since the value could indicate the stability of the perovskite structure. The accepted value is in the region $0.9<t<1.1$ [34]. The value can be calculated approximately by using eqn. (4.1)

$$t = \frac{R_A + R_O}{\sqrt{2}(R_B + R_O)} \tag{4.1}$$

where $R_A$ = the ionic radii of cation A,

$R_B$ = the ionic radii of cation B,

$R_O$ = the ionic radii of anion oxygen.

For BNZ compound, the calculated tolerance factor was 0.92. This showed that the perovskite stability of this system was similar to the well-known perovskite

ceramics, i.e. $BaTiO_3$ (≈1.02), $BaZrO_3$ (≈1), $PbTiO_3$ (≈0.98), $PbZrO_3$ (≈0.96) and $Bi_{0.5}Na_{0.5}TiO_3$ (≈0.968) [35].

### 4.1.1 TG-DSC analysis

Figure 4.1 displays thermal transformation of $Bi_{0.5}Na_{0.5}ZrO_3$ mixed powder using TG-DSC analysis. DSC measurement revealed that there were both endothermic and exothermic transformations during the thermal processing of this compound. The endothermic peak at a low temperature of 300°C was believed to be evaporation of some organic substances present in the powder during mixture preparation. Also, a little weight loss (≈1.44 %) was found in TG curve. In case of the exothermic one observed at high temperature (≈640°C), the transformation was expected to be attributed to a solid-state reaction of BNZ crystallization. Besides, weight loss (~4.09%) in a temperature range of 600 to 800°C seemed to be carbon dioxide ($CO_2$) gas disintegration during BNZ phase formation as shown in the eqn. (3.1) since the gas decomposed at temperature above 600°C [36]. The calcination temperature range of 700, 750, 800 and 850°C was examined in BNZ powder synthesis.

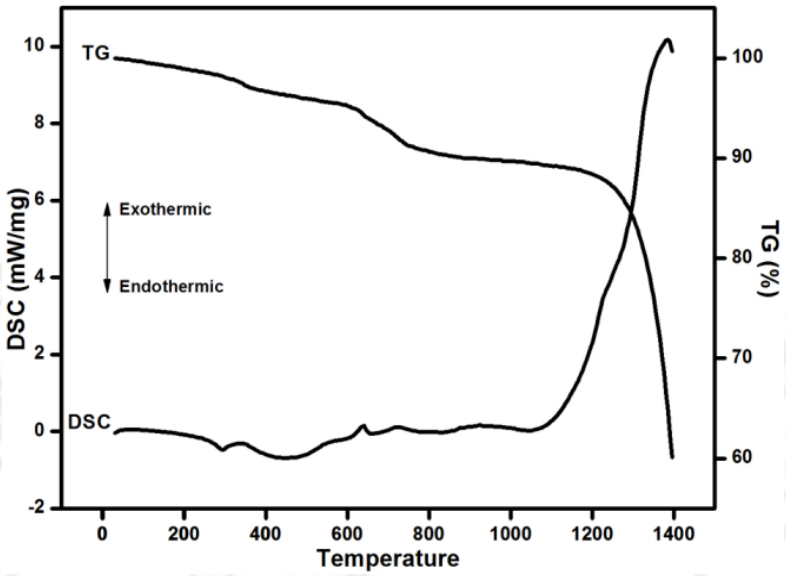


**Figure 4.1** TG-DSC curve of the mixed starting powders.

### 4.1.2 Effects of calcination temperature

X-ray diffraction patterns of BNZ powder calcined at different temperatures as compared with the starting powder are shown in Fig. 4.2. It could be seen that the phases of all the starting oxides existed at 700˚C. This suggested that the mentioned temperature was too low to form complete BNZ phase. With increasing temperature, $Bi_2O_3$ and $ZrO_2$ phase existence was still observed in the powder. However, the secondary phase decreased with the increasing calcinaton temperature up to 800˚C. In case of the calcined powder at 850˚C, the material began to partially melt and react with alumina crucible causing increment of the un-desired phase. Based on this result, it indicated the effect of calcination temperature on BNZ phase formation. Due to lowest secondary phase contamination, it could be mentioned that the optimized calcination temperature was at 800˚C. In additions, the numerical data of weight loss measured in calcination experiment at 800˚C (~4.24%) was in agreement well with

the weight loss observed in TG analysis in Fig. 4.1. This was supported further with that of $CO_2$ release (eqn. 3.1). From this study, it was assumed that the calcination time was insufficient for BNZ complete crystallization. Hence, the effect of calcination time at 800°C on the phase formation was examined in later section.

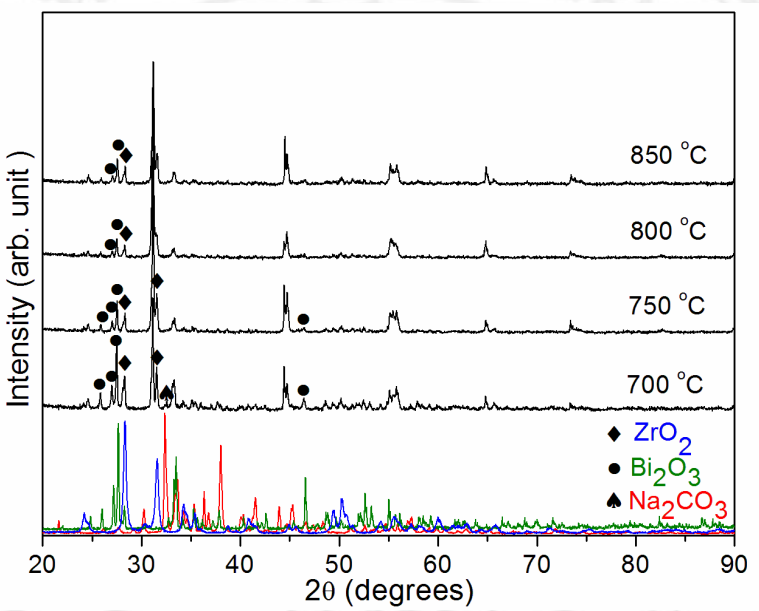


**Figure 4.2** X-ray diffraction patterns of BNZ powders calcined at 700-850°C.

### 4.1.3 Effects of calcination time

X-ray diffraction patterns of BNZ powder calcined at 800°C for 2, 4, 6 and 8 h are shown in Fig. 4.3. It was found that the amount of secondary phase decreased with increasing the calcination time. Nonetheless, the phases of starting powders ($Bi_2O_3$ and $ZrO_2$) were still seen in all powders calcined at various times. In the samples calcined at 6 and 8 h, the partially-melted powder was observed due to the increasingly-accumulated heating with the increasing time. From this result, it was evident that the calcination time could not approach BNZ single phase. Further

observation indicated that $Bi_2O_3$ and $ZrO_2$ presence could be seen in all samples whereas $Na_2CO_3$ was not found. It was possible that $Na_2CO_3$ was deficient during the reaction. The hypothesis, which related the starting powder deficiency, was subsequently demonstrated in later section.

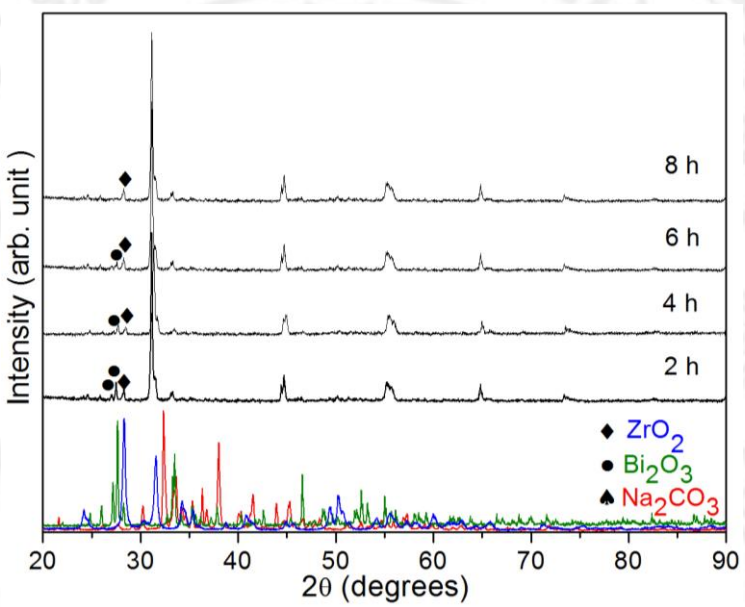


**Figure 4.3** X-ray diffraction patterns of BNZ powder calcined at 800°C for 2-8 h.

### 4.1.4 Effects of excess starting powders

X-ray diffraction patterns of BNZ/$x$$Na_2CO_3$ powders where $x$ = 0, 5, 10 and 15 wt% that were calcined at 800°C for 2 h are shown in Fig. 4.4. It was found that the secondary phase decreased for the modification of $x$ = 5 wt% and did not exist in the powder with $x$ = 10 and 15 wt%. The result suggested that $Na_2CO_3$ addition at 10 wt% and more could complete the BNZ reaction. However, in order to demonstrate the influence of $Na_2CO_3$ deficiency during the calcination process on BNZ phase formation, the $Bi_2O_3$ and $ZrO_2$ addition i.e. BNZ/$Bi_2O_3$ and BNZ/$ZrO_2$ powders were further carried out in this study. Figure 4.5 and 4.6 present XRD results of

BNZ/$x$$Bi_2O_3$ and BNZ/$x$$ZrO_2$ powder where $x$ = 0, 5, 10 and 15 wt% that were calcined at 800°C for 2 h, respectively. It could be noticed that the undesired phases still existed in all powders. Moreover, its amount seemed to rise with increasing addition. This supported obviously that $Na_2CO_3$ deficiency affected significantly BNZ crystallization process which resulted in the existence of $Bi_2O_3$ and $ZrO_2$. Based on powder preparation in this work, it could be deduced that the powder fabricated from the optimized condition i.e. BNZ/10wt%$Na_2CO_3$ sample calcined at 800°C for 2 h was the representative BNZ material in the following investigation.

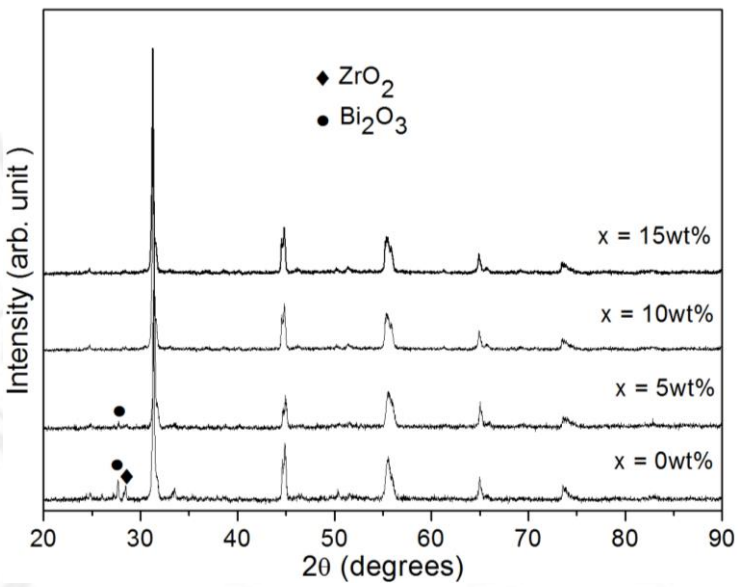


**Figure 4.4** X-ray diffraction patterns of BNZ/$x$$Na_2CO_3$ powders.

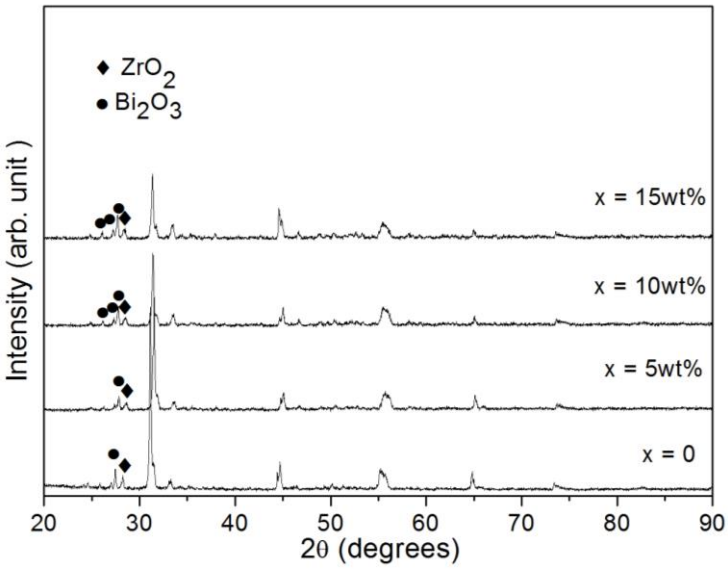


**Figure 4.5** X-ray diffraction patterns of BNZ/$x$$Bi_2O_3$ powders.

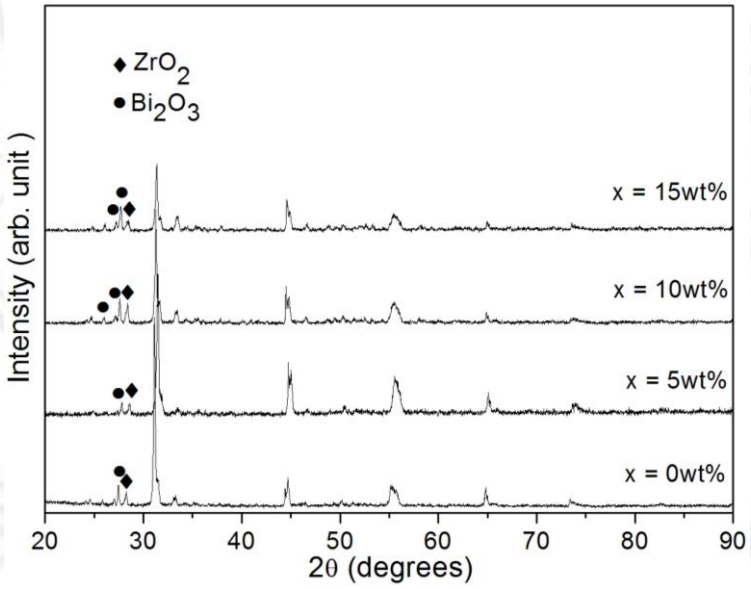


**Figure 4.6** X-ray diffraction patterns of BNZ/$x$$ZrO_2$ powders.

### 4.2 BNZ powder morphology and chemical composition

The powder morphology of BNZ observed using the scanning electron microscopy (SEM) is shown in Fig. 4.7(a). It could be observed that most of the particles were circular and agglomerated due to surface energy reduction. Fig. 4.7(b) presents BNZ initial powder size obtained from its own SEM image, indicating the size in a range of 0.35 to 0.9 μm. The average particle size could be divided into 2 sizes i.e. 0.4 and 0.75 μm. According to this observation, the data seemed to suggest the non-uniform particle size distribution of this material. A selected area of the powder studied using energy dispersion X-ray analysis (EDX) technique are shown in Fig. 4.8 and the chemical composition are listed in Table 4.1. It was found that the powder consisted mainly of Bi, Na, Zr and O elements, which are based elements of BNZ system.

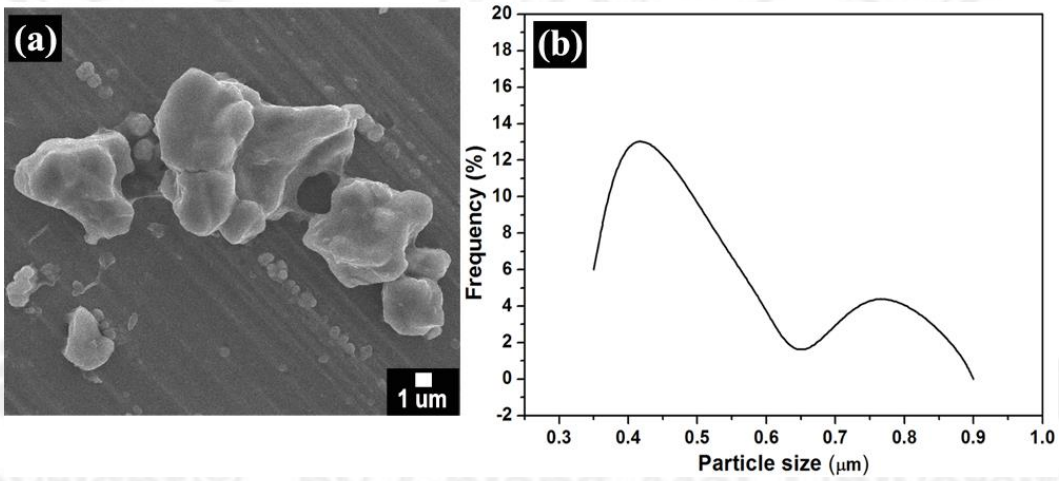


**Figure 4.7** BNZ powder characterization (a) powder morphology (b) particle size distribution.

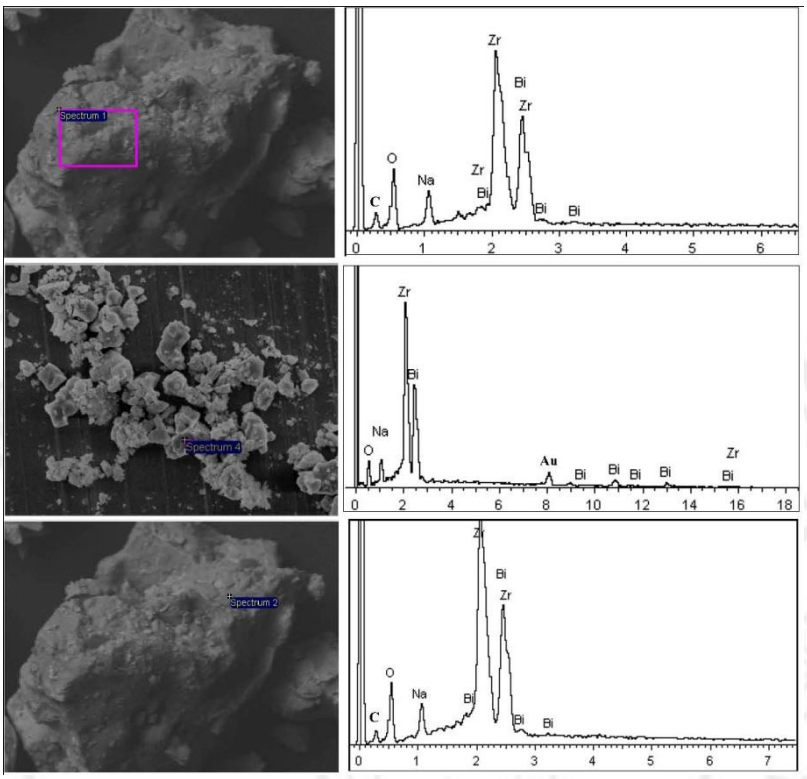


**Figure 4.8** EDX analysis of BNZ powder.

**Table 4.1** Chemical composition of BNZ powders.

| Elements | Detected atomic (%) |
|---|---|
| Bi | 11.41 ± 0.49 |
| Na | 11.21 ± 2.28 |
| Zr | 20.04 ± 3.46 |
| O | 57.35 ± 2.43 |
| Total | 100 |

### 4.3 BNZ Crystal structure investigation

The optimized powder was used for the crystal structure investigation of $Bi_{0.5}Na_{0.5}ZrO_3$ material employing Powder Cell Software [33]. Figure 4.9 presents the fitting result between the calculated pattern by the software and the observed pattern by the X-ray diffraction analysis. The final output after the refinement revealed that this lead-free powder possessed an orthorhombic perovskite structure, in good

agreement with the literature report of Lily et al. [5]. The general crystal structure details belonging to BNZ powder are listed in Table 4.2.

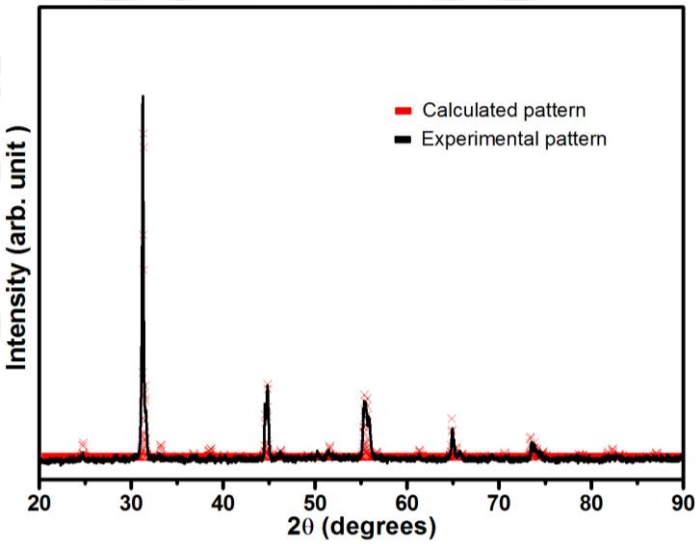


**Figure 4.9** Fitting result of BNZ powder by Powder Cell Software.

**Table 4.2** Crystal structure data of BNZ powders.

| Lattice parameters | Values |
|---|---|
| space group | pnma |
| a axis | 5.7794 Å |
| b axis | 8.1615 Å |
| c axis | 5.7022 Å |
| cell volume | 268.96 $Å^3$ |
| theoretical density | 6.312 $g/cm^3$ |

### 4.4 BNZ ceramic fabrication

In this section, BNZ dense ceramic fabrication was pointed out. The effects on the ceramic processing were divided into four parts which included the effects of sintering temperature, sintering time, initial particle characteristic as well as sintering aids. The relationship of these processing factors and BNZ phase, microstructure and density was discussed in detail.

### 4.4.1 Effect of sintering temperature

The conventional sintering technique was used to fabricate $Bi_{0.5}Na_{0.5}ZrO_3$ ceramics at temperatures of 850, 900, 950, 1000, 1050 and 1100˚C for 2 h in a covered alumina plate with a heating/cooling rate of 5˚C/min. Before and after sintering process, dimension and weight of the green bodies and sintered pellets were measured in terms of volume shrinkage and weight loss, respectively. The tendencies of the both calculated values are illustrated in Fig. 4.10. The graph showed the trends of volume shrinkage (dash line) and weight loss (solid line), which increased gradually for 850-950˚C and rapidly for beyond 1000˚C, respectively. As for the abrupt increment, it was due to the fact that, higher temperature resulted in large shrinkage and also compositional degradation of the sintered samples, particularly, $Bi_2O_3$ at 825˚C [37] and $Na_2CO_3$ at 600˚C [36]. Further observation showed that partial melting was observed to begin at 1000˚C.

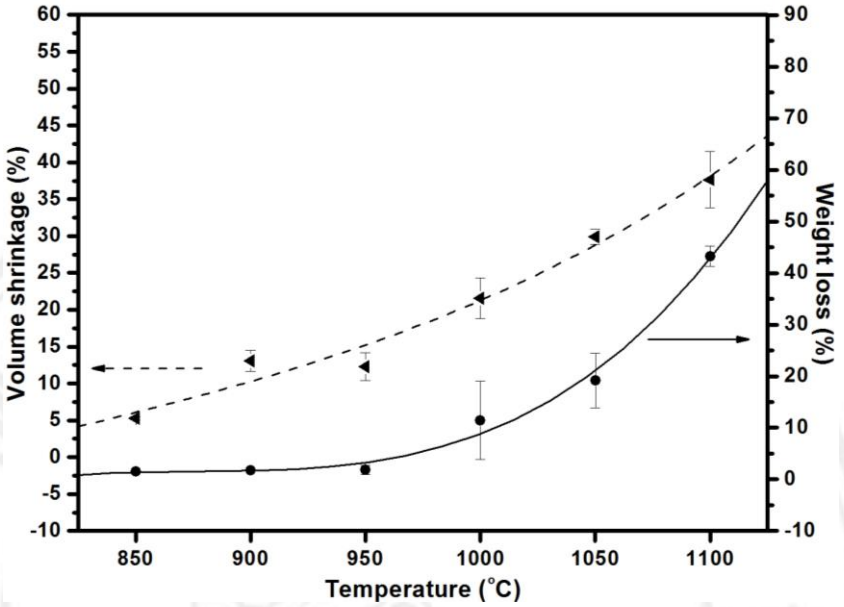


**Figure 4.10** Volume shrinkage and weight loss of BNZ ceramics with different temperatures.

After the physical measurement, the phase characteristic of all polycryatalline BNZ was identified employing X-ray diffraction technique. Figure 4.11 shows XRD patterns of BNZ ceramics sintered at different temperatures. It could be seen that all patterns, except the condition sintered at 1100°C, were similar to that of BNZ calcined powder as shown in section 4.3. These sintered samples were confirmed apparently to be orthorhombic perovskite. However, the sintering temperature significantly affected purity of BNZ ceramic phase. At 850 and 900°C, the polycrystalline sample exhibited a complete solid solution with the orthorhombic phase. At 950 to1100°C, $ZrO_2$ starting compound phase (MDI/JADE9 No. 000371484) was found and increased with increasing temperature. As a result, the compounds having low melting points, i.e. $Bi_2O_3$ and $Na_2CO_3$, were expected to cause the mentioned secondary phase

existence. This was correlated well with those of the high weight loss values in Fig. 4.10.

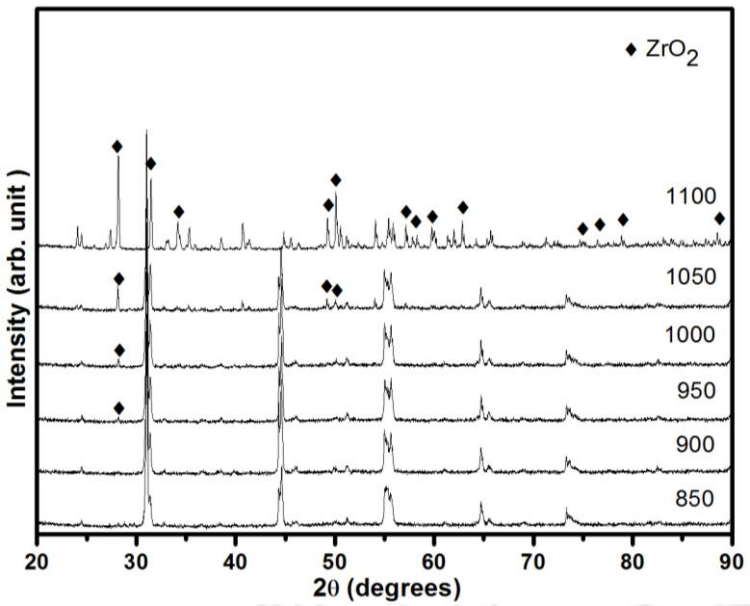


**Figure 4.11** XRD patterns of BNZ ceramics with different temperatures.

Figure 4.12 displays the microstructure of BNZ ceramics sintered at different temperatures. The images indicated that the crystalline grain size of 2-7 μm. Besides, the BNZ average grain increment was observed with increasing temperature. As the result, the higher sintering temperature was expected to have sufficiently high energy providing the easier atomic diffusion and grain growth during the initial and intermediate state sintering, respectively, than the lower sintering temperature. Nonetheless, porous structure was found at all sintering temperatures and it increased when the temperature increased. In particular, the ceramic sintered at highest temperature showed a large pore size and high porosity. It was possibly due to the compositional degradation of $Bi_2O_3$ and $Na_2CO_3$, in good agreement with weight loss value and the secondary phase existence in XRD result. The relative densities as a

function of sintering temperature of all BNZ ceramics are presented in Fig. 4.13. The value increased with temperature increment up to 1050˚C, reaching the maximum value of about 75%, but the value decreased dramatically at highest sintering temperature. Its own microstructures were associated well with the densities. However, the density of BNZ using the mentioned sintering temperature was rather poor (i.e. relative value ~ 68-75%). Also, it produced $ZrO_2$ rich phase at temperature 950˚C and higher. The results guided that varying only the sintering temperature did not reach BNZ dense ceramic. Based on this study on the effects of the sintering temperature on BNZ ceramic fabrication, it could be mentioned that the temperature used to sinter BNZ ceramic should be either 850 or 900˚C. In later section, the effect of sintering time at 900˚C would be studied and discussed because this temperature did not produce secondary phase and the density of the ceramics was higher than the sample sintered at 850 ˚C.

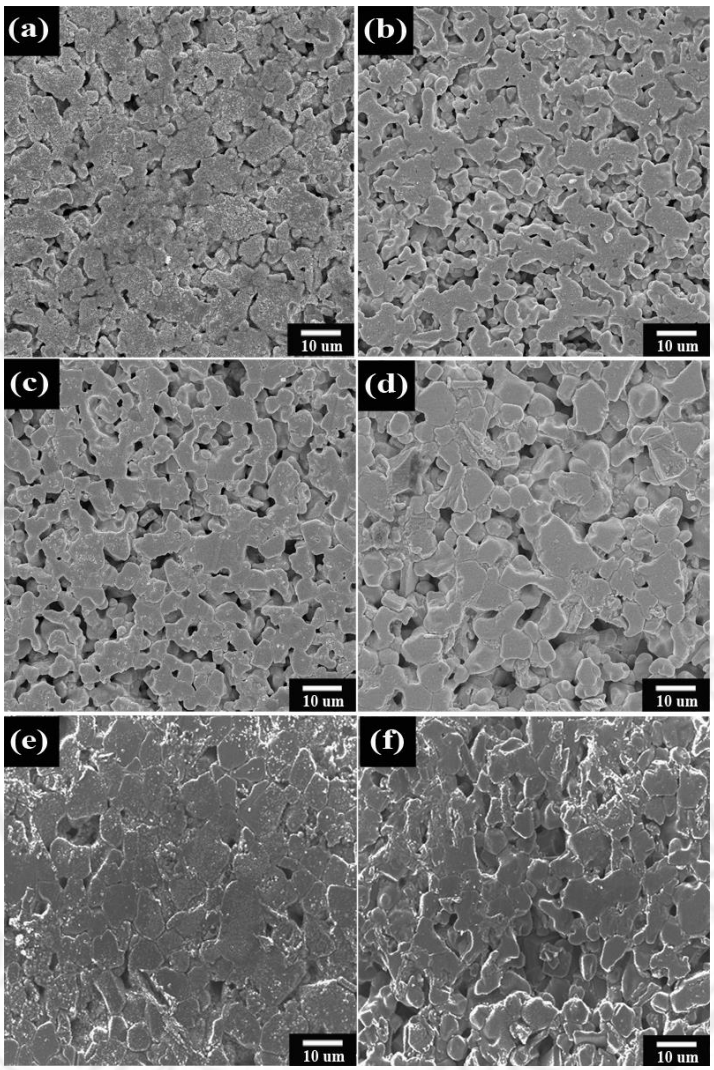


**Figure 4.12** SEM images of BNZ ceramics with different temperature where a = 850, b = 900, c = 950, d = 1000, e = 1050 and f = 1100˚C.

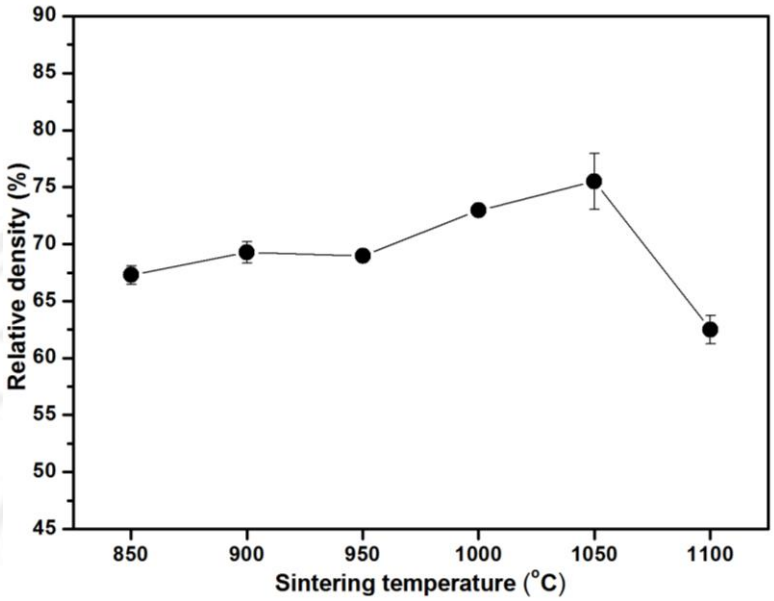


**Figure 4.13** Relative densities of BNZ ceramics with different sintering temperatures.

### 4.4.2 Effect of sintering time

The plot of quantitative densification data of BNZ ceramics sintered at 900°C with different time, i.e. 2, 4, 6 and 8 h are shown in Fig. 4.14. It could be observed that the trends of both shrinkage and weight loss increased with increasing time. Regarding the volume shrinkage, this increasing tendency was quite small as compared with that of sintering temperature factor (Fig. 4.10). This might indicate that the influence of the sintering temperature was greater than the sintering time on this material. In case of weight loss, the detail showed the same behavior.

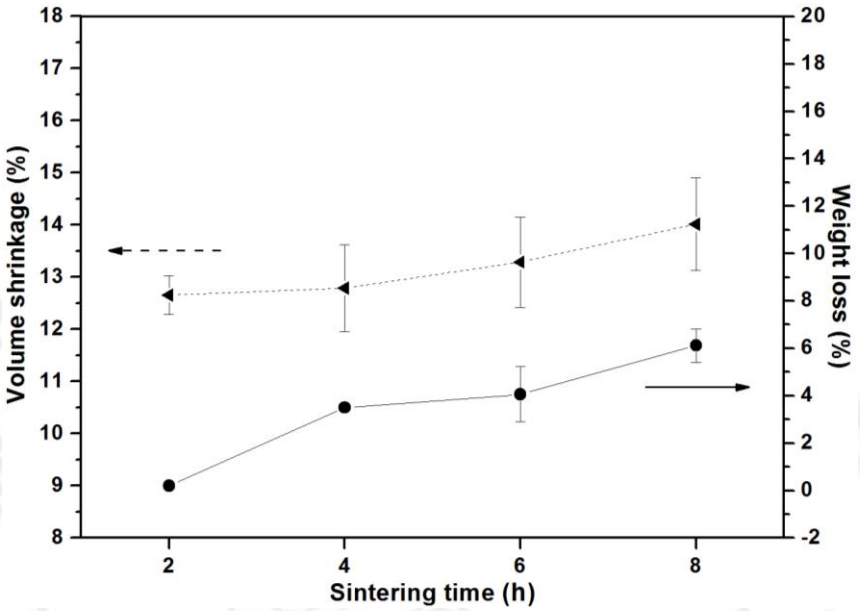


**Figure 4.14** Volume shrinkage and weight loss of BNZ ceramics with different time.

X-ray diffraction patterns of BNZ ceramics sintered at several sintering times are shown in Figure 4.15. This analysis revealed that all the samples possessed the orthorhombic phase structure. However, the extra secondary phase presence of $ZrO_2$ was noticeable with the sintering time of 6 and 8 h, but the intensity was weak in the sample sintered for 4 h. This evidence confirmed apparently the compositional degradation of $Bi_2O_3$ and $Na_2CO_3$ during firing. Among these samples, the one sintered for shortest time showed only the orthorhombic phase without the secondary contamination. Figure 4.16 plots the relationship between the relative densities of BNZ ceramics and the sintering time. It could be seen that the value tended to increase with increasing time. The maximized density (~ 75%) was found in the sample sintered at the longest time. Compared to the widely-accepted relative density value (≥ 95%), BNZ density, which was obtained by variation of sintering temperature and time factors, was rather low (~ 70 - 75%). This revealed that both

factors could not produce BNZ dense ceramic. However, the optimum firing condition for this material at temperature ≤ 900°C for 2 h was revealed in this study. Another factor which was BNZ powder characteristics with non-uniform particle size distribution found in the section 4.2 possibly had some influence on the densification of this material. Hence, effect of initial particle characteristic was subsequently examined in next section.

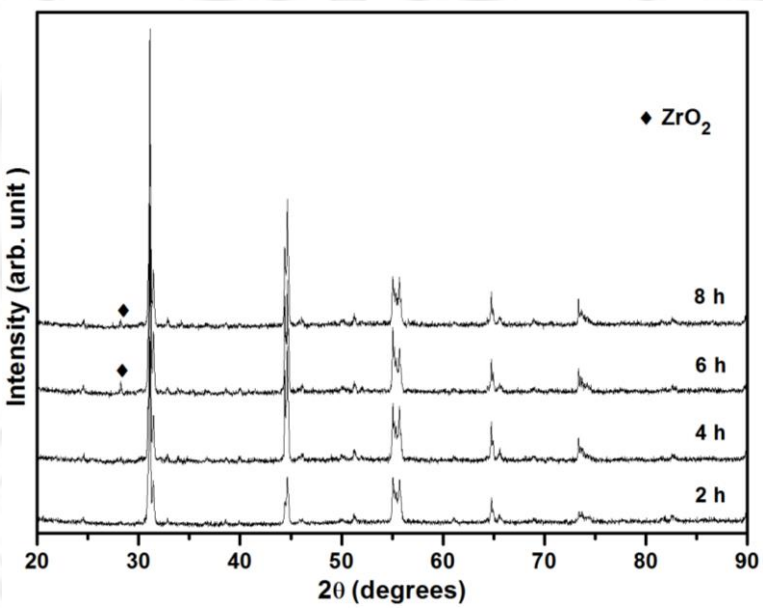


**Figure 4.15** XRD patterns of BNZ ceramics sintered at different sintering time.

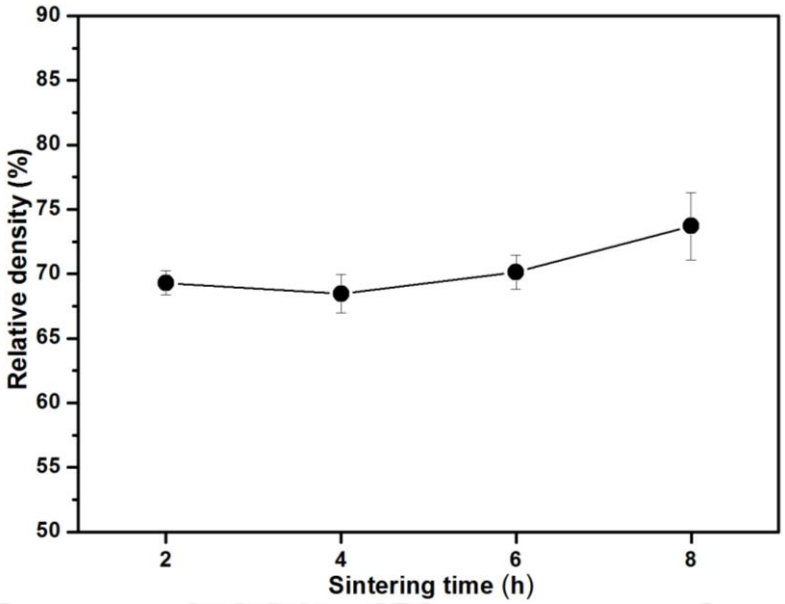


**Figure 4.16** Relative densities of BNZ ceramics sintered at different time.

### 4.4.3 Effect of initial particle characteristic

In this section, the ball milling process of BNZ calcined powder for 0, 24, 48, 72 and 96 h was carried out in order to investigate the effects of powder characteristics on its ceramic fabrication (abbreviated hereafter as BNZ0, BNZ24, BNZ48, BNZ72 and BNZ96, respectively). Figure 4.17 shows X-ray diffraction patterns of the calcined powder with different milling time. It could be noticed that all powders indicated similar XRD patterns and contained no extra peaks. This clearly assured that the milling process did not cause contamination in this powder and all sample maintained the orthorhombic perovskite phase. Figure 4.18 shows the effect of the milling process on the lattice parameters of BNZ powder. The data indicated that there was not any significant change in axis a (blue solid line), b (red dot line) and c (green dash line) with increasing milling time. This confirmed that this process did not affect importantly the BNZ structure. However, this mechanical process was found to influence significantly the crystallite size and microstrain within BNZ

lattices. The mentioned effect would be discussed together with its ceramic in later section.

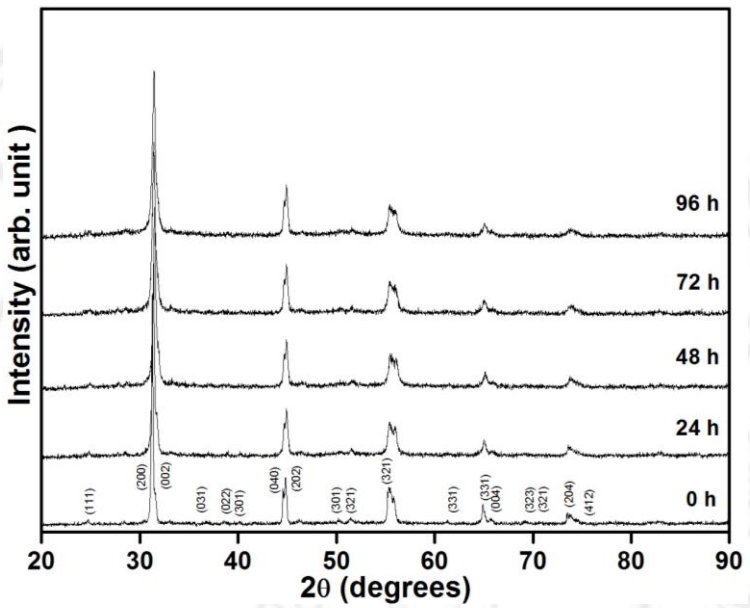


**Figure 4.17** XRD patterns of BNZ powder with different milling time.

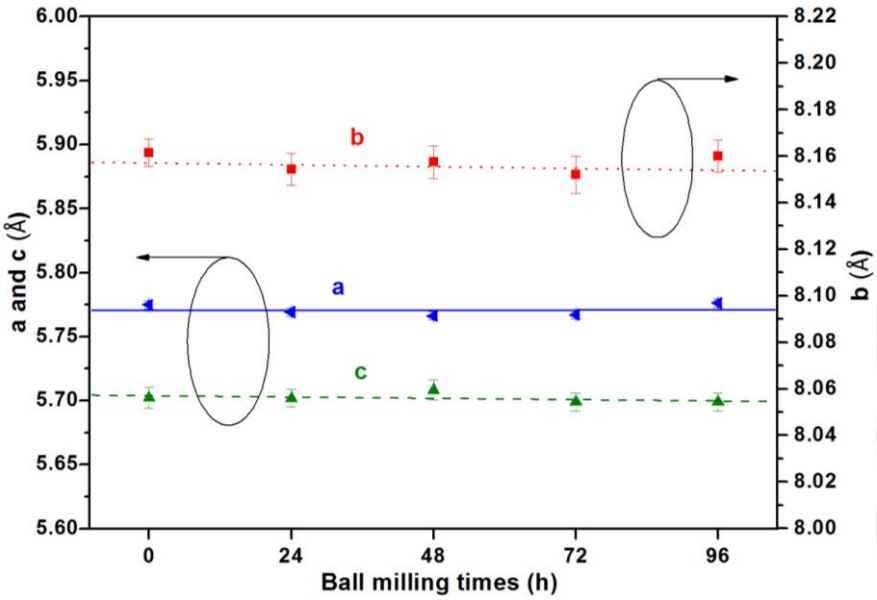


**Figure 4.18** Lattice parameters of BNZ powder at different milling time.

Figure 4.19 illustrates BNZ powder morphologies with several milling times, i.e. 0, 24, 48, 72 and 96 h. For the powder without modification (i.e. as calcined powder), it could be observed that the particles were round or smooth surface and there were several particle sizes (wide particle size distribution). When milling time increased, the particle size decreased obviously. The frequency distribution of BNZ particle size for different ball milling time of 0, 24, 48, 72 and 96 h are plotted in Figure 4.20. It could be seen that the un-ground BNZ sample exhibited large average sizes (0.4 and 0.75 μm) and broad particle size distribution (0.35-0.9 μm). When the milling time was increased, the mentioned features gradually changed into finer powder sizes with narrower size distribution. Nonetheless, further changes could not be seen in BNZ72 and BNZ96 powders, suggesting the limitation of the conventional ball milling process in modifying the BNZ powder characteristics. Observation in the powders with longest milling time also indicated the existence of two-peak curves, suggesting the effect of powder agglomeration due to surface energy reduction. The SEM images (Fig. 4.19) were consistent with the results of particle size distribution and mean particle size measurements.

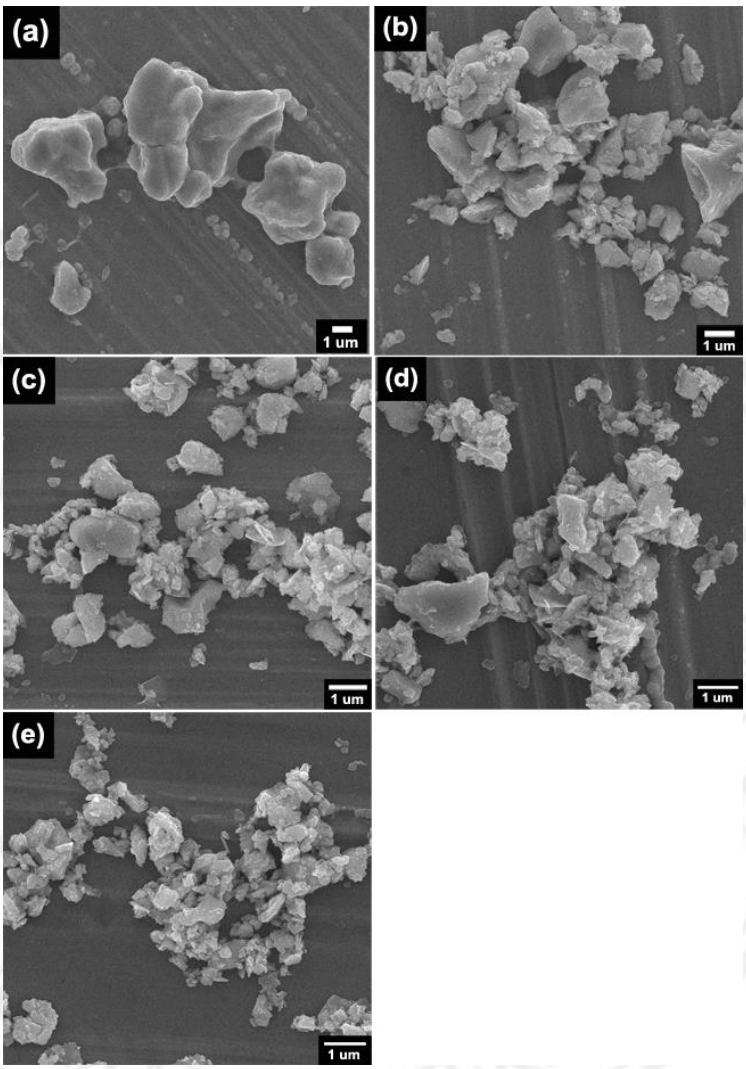


**Figure 4.19** BNZ powder morphologies with different ball milling time where a = 0, b = 24, c = 48, d = 72 and e = 96 h.

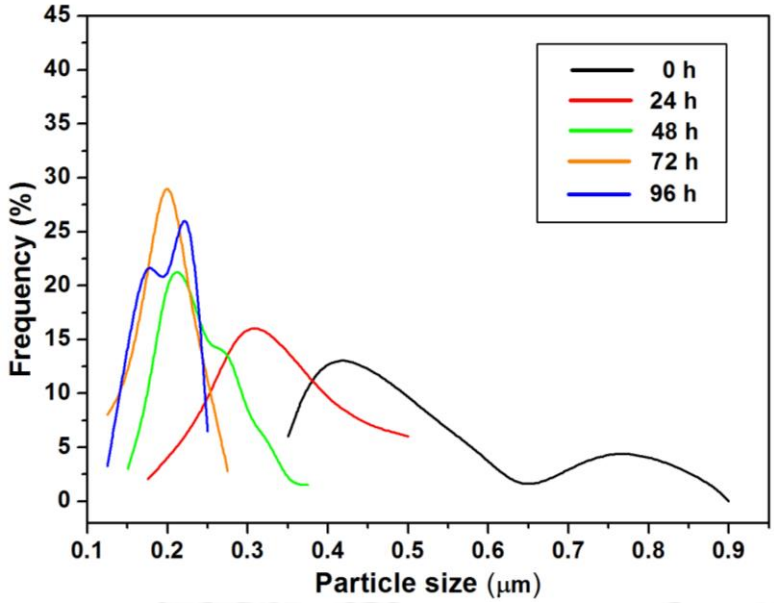


**Figure 4.20** Frequency distribution of BNZ particle size with different ball milling time.

For the investigation of the effects of initial particle characteristic in BNZ ceramic fabrication, the sintering condition at 900°C for 2 h was chosen to prepare the samples due to the fact that sample prepare under this condition (section 4.41 and 4.42) showed optimized density and phase purity. Volume shrinkage and weight loss data of the ceramics are shown in Fig. 4.21. For the weight loss, the values of all samples were not different and did not show any significant trend. On the other hand, the shrinkage increased rapidly at ball milling time 48 and 72 h and then did not change at the highest milling time. This seemed to guide that the initial particle characteristic might affect significantly the ceramic densification. Phase identification of the sintered specimens at 900°C, as displayed in Fig. 4.22, also indicated that all ceramics were single orthorhombic phase. Thus, it was clearly confirmed that the ball milling process did not have any influence on crystallographic form of BNZ ceramics.

Figure 4.23 represents the lattice parameters of BNZ ceramics produced from the powder with different ball milling times. It was observed that the milling process did not result significantly BNZ ceramic lattice parameters, which was in good agreement with its powder result as shown in 4.18. However, Fig. 4.24 revealed the effect of milling time on crystallite size and microstrain of the powders and ceramics whose values were obtained from eqn. (4.2).

$$B\cos\theta = \frac{K\lambda}{D} + 2(\varepsilon)\sin\theta\,, \qquad (4.2)$$

where $B$ is the full width at half maximum (FWHM) of the XRD peaks, $K$ the Scherrer constant, $D$ the crystallite size, $\lambda$ the wavelength of the X-ray, $\varepsilon$ the lattice strain, and $\theta$ the Bragg angle.

It was obvious that the crystallite size of the powders decreased significantly when the ball milling time increased from 0 to 48 h, and only slightly decreased during 72-96 h milling time. The mentioned crystallite size reduction induced some strain in the powders and the amount of internal microstrain increased accordingly with the milling time increment. On the other hand, for all fired ceramic samples, the internal strain was found to be close to zero and did not depend on milling time. Based on the results, it seemed that the temperature of 900°C was enough to completely relieve the accumulated internal microstrains within the ground powders, leading to the observed crystallite size increase of the ceramics as compared with the powders with the same milling time. There were some similar reports in the literature on the effect of ball milling time on crystallite size and lattice strain [38, 39].

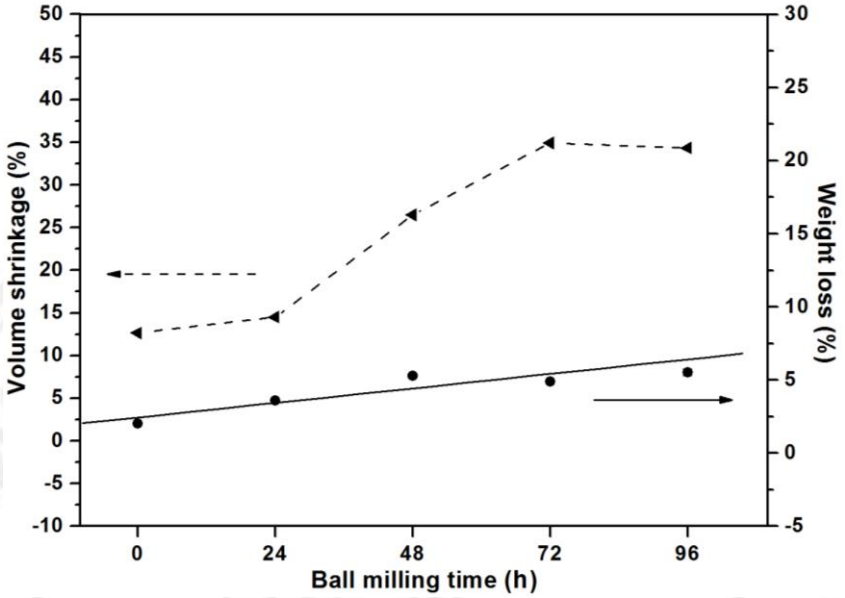


**Figure 4.21** Volume shrinkage and weight loss of BNZ ceramics with different ball milling time.

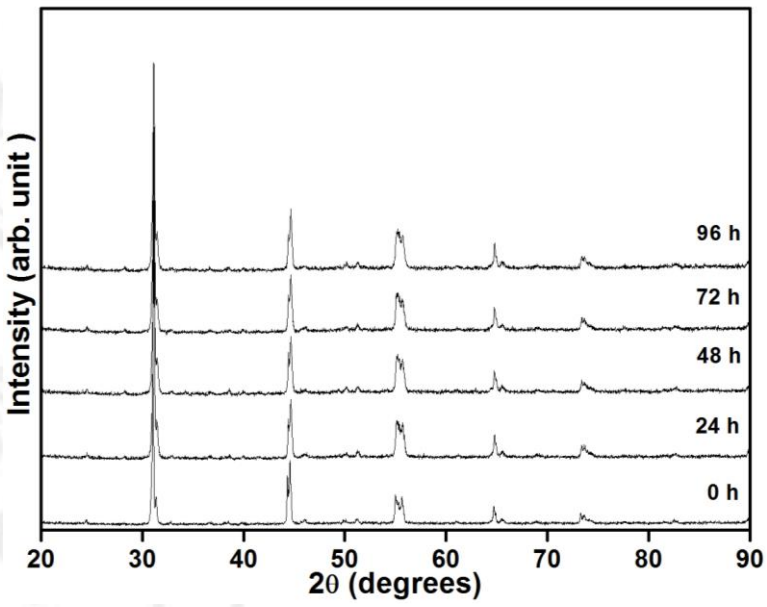


**Figure 4.22** XRD patterns of BNZ ceramics with different milling time.

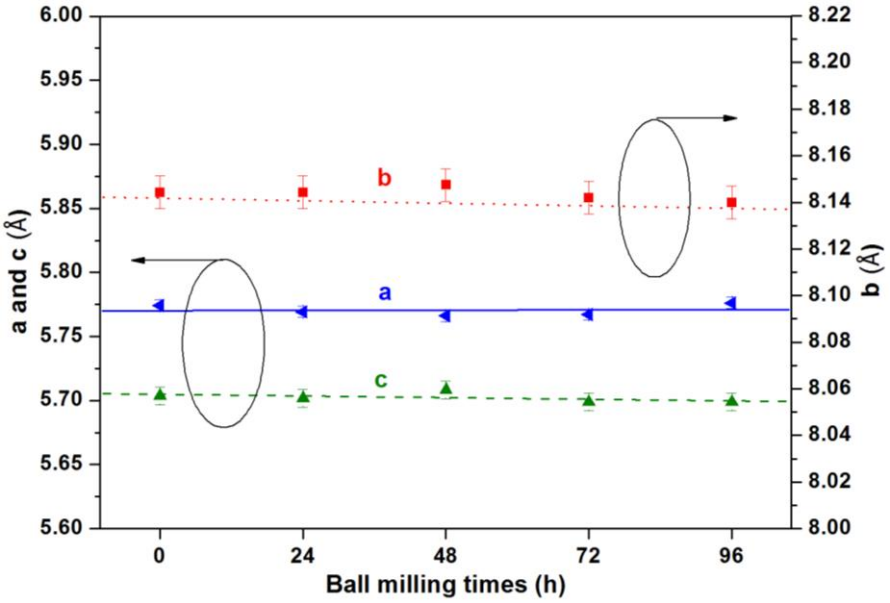


**Figure 4.23** Lattice parameters of BNZ ceramics at different milling time.

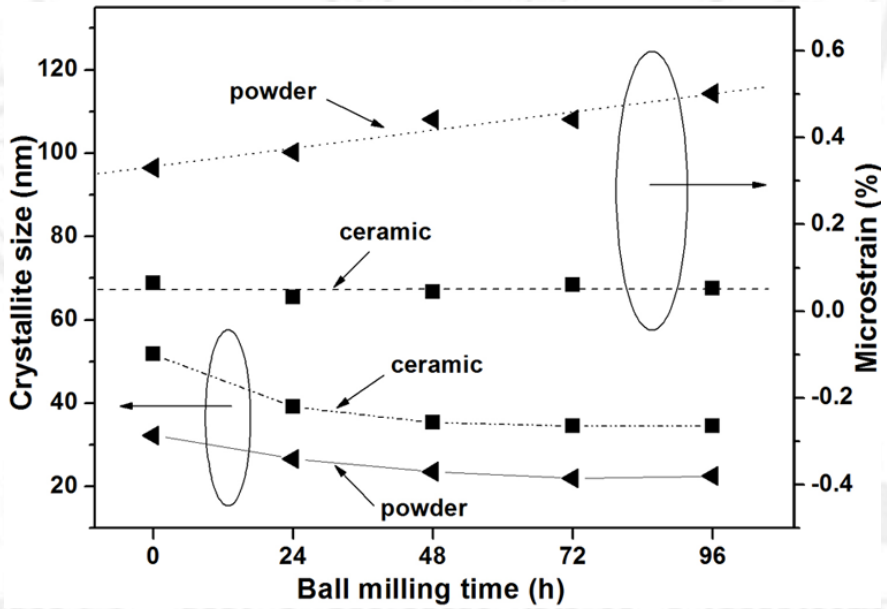


**Figure 4.24** Crystallite size and microstrain of BNZ powder and ceramics at different milling time.

SEM images of BNZ sintered specimens at 900°C for 2 h are presented in Fig. 4.25. It could be noticed that the un-ground sample was composed of the crystalline grain (~ 4-5 μm), porous structure and non uniform grain size distribution. For the ceramics with ball milling modification, size of BNZ grains decreased with increasing ball milling time. Also, uniform grain distribution was found with the milling time increment. Figure 4.26 illustrates a frequency distribution of grain size of sintered BNZ samples with various milling times of 0, 24, 48, 72 and 96 h. It was evident that BNZ ceramics received from the powder milled at 72 and 96 h with finer powders and more uniform particle size distribution (Fig. 4.20) produced a uniform grain size distribution and fine-grained microstructure because a powder compact with fine particles and uniform size distribution prolonged the intermediate stage of the sintering process, which in turn would inhibit the grain growth in the mentioned stage [40, 41], hence causing a decrease in grain size and an increase in grain uniformity. This result was in good agreement with several reports on uniform and fine-grained ceramics as a result of the starting powder contributions [41-43]. In case of the observed decrease in porosity, it was attributed consequently from the increase of finer and more uniform grain size distribution to facilitate the pore closing during final sintering stage [40, 41].

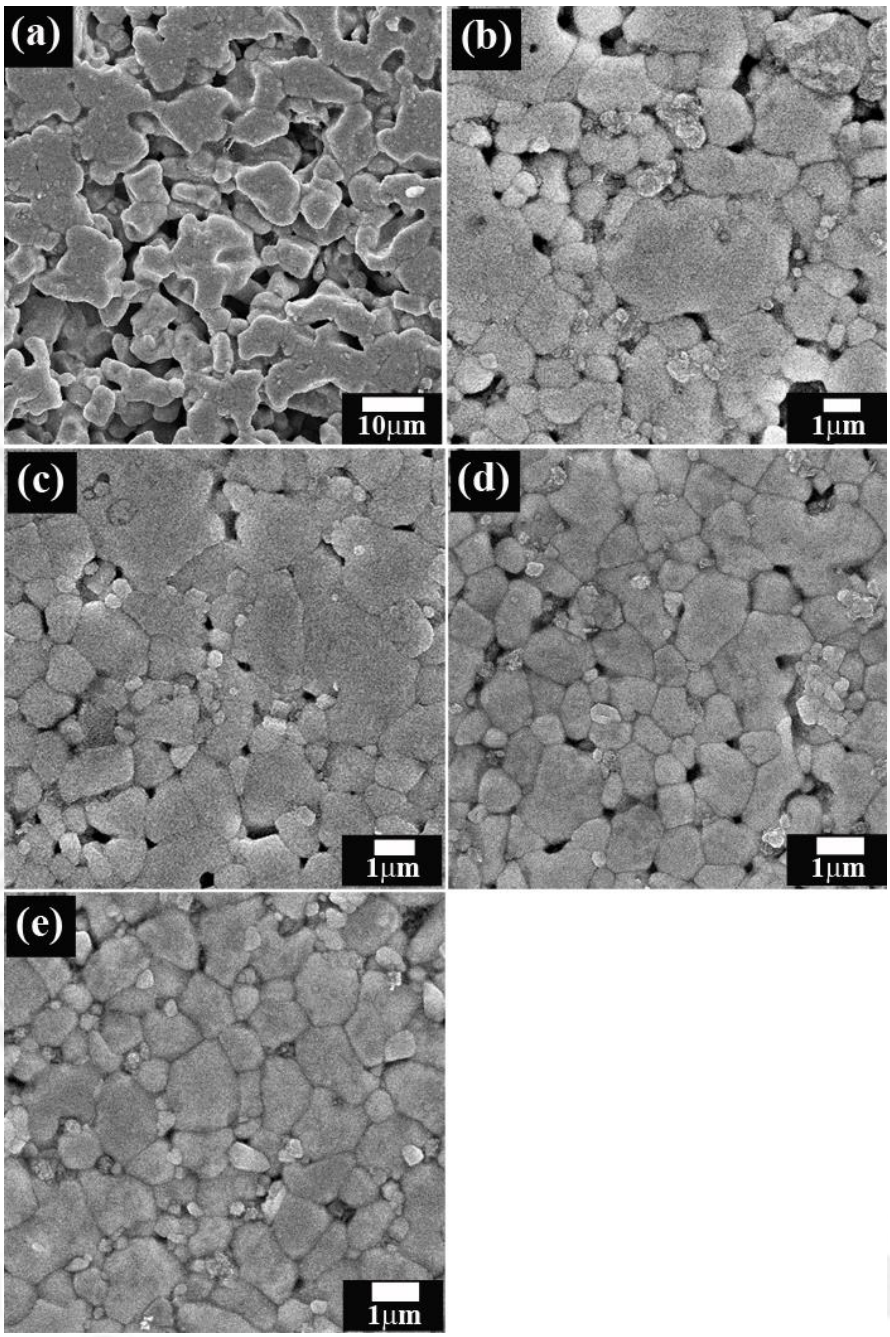


**Figure 4.25** SEM images of BNZ ceramics with different ball milling time where a = 0, b = 24, c = 48, d = 72 and e = 96 h.

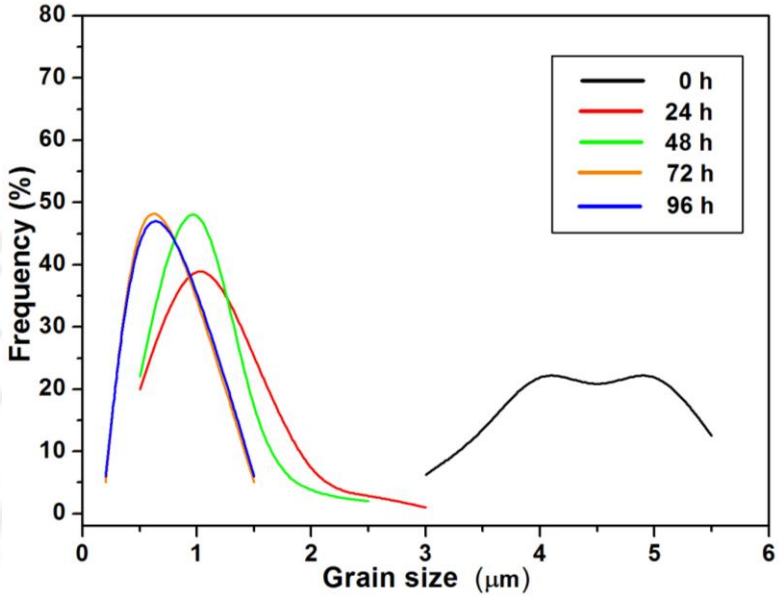


**Figure 4.26** Frequency distribution of BNZ grain size with different ball milling time.

Quantitative density data of all ceramics as a function of ball milling time (black solid line) are given in Fig 4.27. The relative values increased slowly with the milling time up to 48 h but then abruptly increased in the ceramic produced from powders milled for 72 h. However, the relative densities of the ceramics produced from BNZ72 and BNZ96 powders were not significantly different. All of the measured density values were seen to relate directly to respective shrinkage, as shown in Fig. 4.21 and microstructures, as shown in Fig. 4.25. The maximum density value (≈ 85%) was found in BNZ72 ceramic. Nonetheless, the microstructure of the mentioned ceramic was still seen to compose of many pores even though it had a more uniform grain size distribution as compared to the sample produced without additional milling. This seemed to imply that only powder milling process was insufficient to achieve the dense microstructure and the widely-accepted relative density (≥ 95%) for electrical ceramic materials. Based on this study, BNZ optimized powder with 72 h ball milling

time was revealed. Hence, in order to further improve its microstructure and relative density, addition of $Na_2CO_3$ and $Bi_2O_3$ as sintering aids was carried out to help increase the sinterability of BNZ ceramics at the mentioned milling condition in later section, similar to the case of adding PbO to improve PZT microstructural evolution at lower temperature [44, 45].

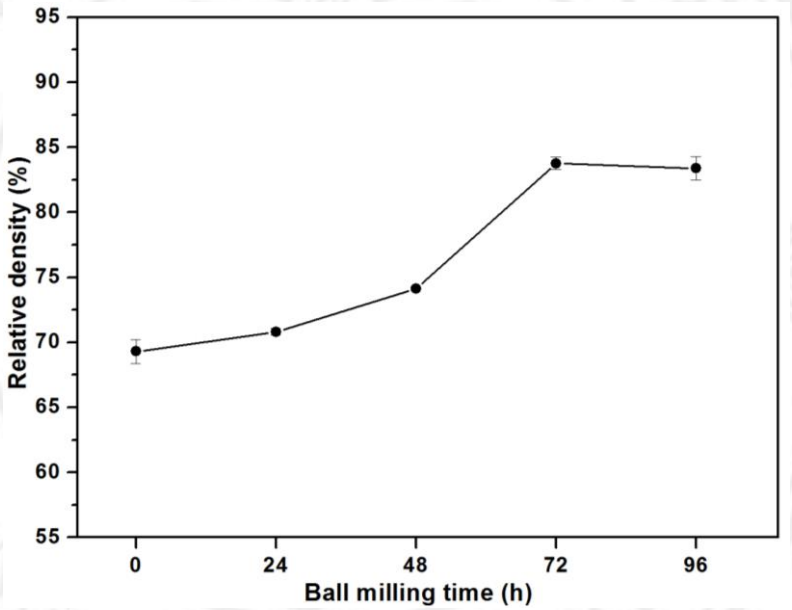


**Figure 4.27** Relative density as a function of ball milling time for BNZ ceramics.

### 4.4.4 Effect of sintering aids

In this study, $Na_2CO_3$ and $Bi_2O_3$ were employed to evaluate BNZ densification at low temperature because both oxides are widely-known as sintering aid to enhance ceramic microstructure [46, 47]. Subsequently, $Na_2CO_3$ and $Bi_2O_3$ were added separately in content of 0, 1, 4, 7 and 10 wt% to the representative powder BNZ72. For the ceramic sintering process, the doped samples were fired at low temperatures (800, 850 and 900°C). Figure 4.28 shows the volume shrinkage and weight loss of the BNZ72/$x$$Na_2CO_3$ samples as a function of $Na_2CO_3$ concentration at several

temperatures. It could be noticed that, at $x < 4$ wt%, the dimensional and weight values increased rapidly (except at 800°C) while, at $x \geq 4$ wt%, the values did not differ significantly. This might imply the influence of this sintering aid on BNZ densification. However, high weight loss (~ 15%) of the ceramics with $x \geq 4$ wt% as compared with that of pure one (~ 3%) was also noticeable at temperature beyond 850°C. The volume shrinkage and weight loss of the BNZ72/$x$$Bi_2O_3$ samples as a function of $Bi_2O_3$ concentration at the temperatures of 800, 850 and 900°C are presented in Fig. 4.29. Regarding the resulted dimension, the addition showed the trend which was similar with the case of $Na_2CO_3$. For comparison of both sintering aids, the observed values of shrinkage BNZ72/$x$$Bi_2O_3$ were higher than that of BNZ72/$x$$Na_2CO_3$ with the same content of about 15%. In terms of weight loss, both pure and $Bi_2O_3$-doped ceramics sintered at all temperatures showed almost the same value in doping range of ~ 1 - 6% meanwhile the values of $Na_2CO_3$-doped samples were different. This result seemed to suggest that $Na_2CO_3$ degradation during the process was easier than $Bi_2O_3$.

Figure 4.30 plots the relative densities of both BNZ72/$x$$Bi_2O_3$ and BNZ72/$x$$Na_2CO_3$ ceramics as a function of sintering aid concentration. $Na_2CO_3$-doped samples (dot lines) would be discussed first. It could be noticed that, at 800°C, the densities increased with increasing $Na_2CO_3$ addition, whereas at 850 and 900°C, the density change could be divided into three regions include at $x \leq 1$ wt% in which the value did not differ significantly, at $x = 4$ wt% in which the value increased rapidly and at $4 < x \leq 10$ wt% where the values were not different. From this result, the data suggested that, at temperature 850 and 900°C, the enhancement of $Na_2CO_3$ sintering aid on BNZ densification with the addition at $x \geq 4$ wt%. However, all values were

lower than that of acceptable value (95%). In case of $Bi_2O_3$-doped samples (solid lines), it was seen that the relative density increased with the addition of $Bi_2O_3$. In samples sintered at 800 °C, the values were still lower than 95%. For the samples fired at 850 and 900°C, it could be noticed that the addition of 1 wt% $Bi_2O_3$ did not affect significantly the density of BNZ ceramic. However, with further modification at $x$ = 4, 7 and 10 wt%, the relative density values dramatically increased closer to the acceptable value (95%) in all samples. These later set of results also showed that the relative densities were almost independent of the sintering temperature and $Bi_2O_3$ content. To compare both cases, the easier and larger degradation of $Na_2CO_3$ (Fig. 4.28) was believed to decrease in BNZ densification while the $Bi_2O_3$ addition with harder and lesser degradation (Fig. 4.29) could elevate the relative density to 95%. Based on this study, it was then concluded that, for the compositions $4 \leq x \leq 10$ wt%, BNZ72/$x$$Bi_2O_3$ ceramics with high relative density could be produced at either 850 or 900°C. Accordingly, the $Bi_2O_3$-doped sample set sintered at lower temperature (850°C) was chosen as representative for further phase and microstructural investigations in the following section.

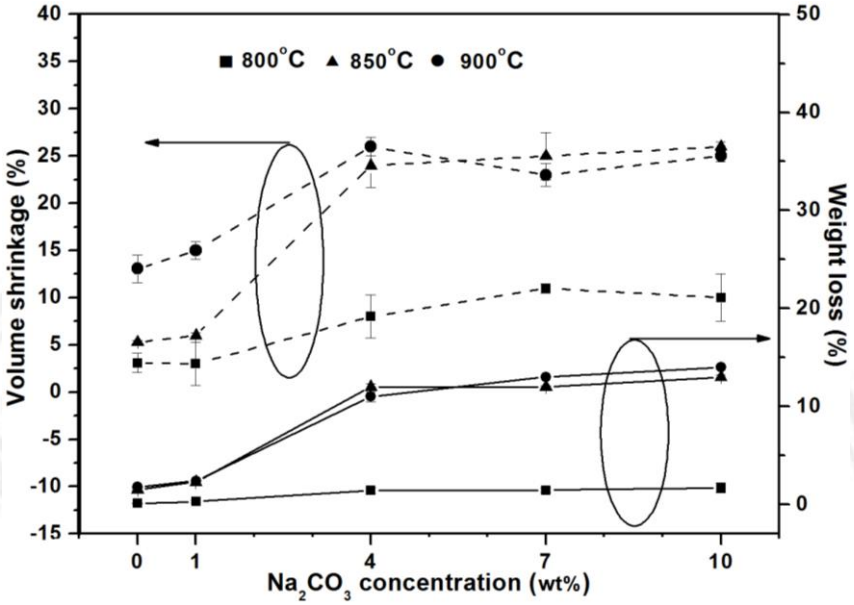


**Figure 4.28** Volume shrinkage and weight loss of BNZ72/$Na_2CO_3$ ceramics with different sintering temperatures.

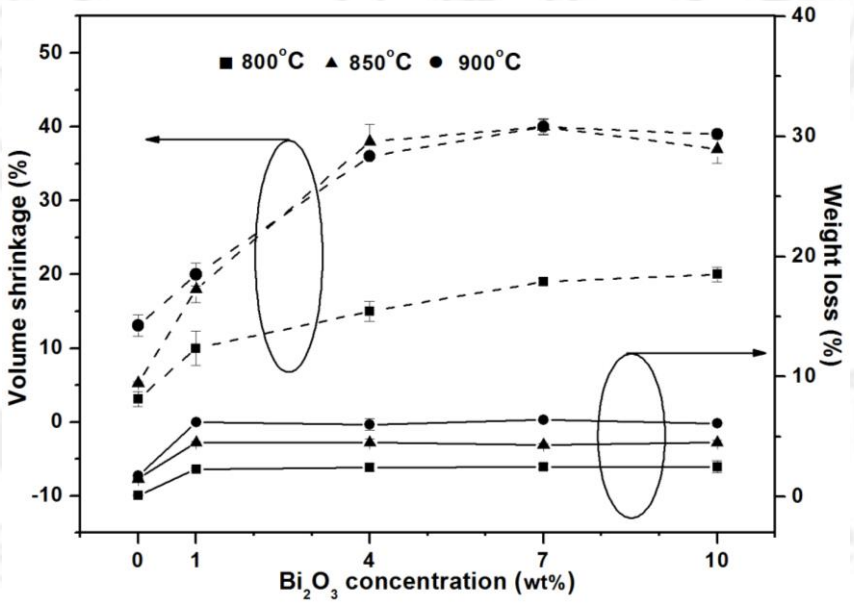


**Figure 4.29** Volume shrinkage and weight loss of BNZ72/$Bi_2O_3$ ceramics with different sintering temperatures.

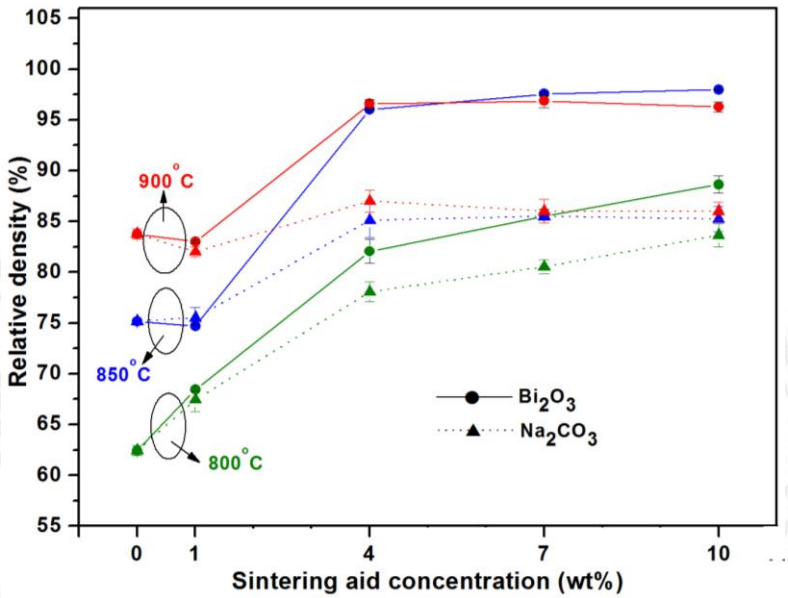


**Figure 4.30** Relative densities of BNZ72/$Na_2CO_3$ and BNZ72/$Bi_2O_3$ ceramics with different sintering temperatures.

XRD diffraction patterns of BNZ72/$x$$Bi_2O_3$ ceramics (sintered at 850°C) where $x$ = 0, 1, 4, 7 and 10 wt% in $2\theta$ range between 20 - 80° are shown in Fig. 4.31. It was observed that both pure and $Bi_2O_3$-added BNZ ceramics possessed the same orthorhombic structure. For the trace of $Bi_2O_3$ sintering aid phase, it exhibited distinctly in the ceramics with $x$ = 7 and 10 wt%. Besides, a weak peak of $Bi_2O_3$ was also observed in the sample containing $x$ = 4 wt%. Figure 4.32 presents the lattice parameters of all the ceramics. The values did not show the $Bi_2O_3$-addition dependence. Thus, it confirmed that the modification by using sintering aid did not affect the BNZ unit cell. SEM micrographs of BNZ72/$x$$Bi_2O_3$ ceramics where $x$ = 0, 1, 4, 7 and 10 wt% and sintered at 850°C are shown in Fig. 4.33. The grain size in the BNZ ceramics with $x \geq 4$ wt% was seen to significantly increase (clearly about 2 μm difference) compared to the BNZ ceramics with $0 \leq x \leq 1$ wt%. The grain size

increment was resulted directly from $Bi_2O_3$ addition which became liquid phase at high temperature and provided high atomic mobility and diffusion during the sintering process, inducing appreciable grain growth rate and pore-filling mechanism. This then increased the shrinkage and relative density of the ceramics with $x$ = 4, 7 and 10 wt%, as shown in Figure 4.29 and 4.30, respectively. Similar microstructural evolution could be found in other ceramics using $Bi_2O_3$ as sintering aid [46, 47]. Further observations from SEM micrographs in Figure 4.33 (d) and (e) indicated inhomogeneous regions (white and gray areas). EDX analysis of the selected ceramic BNZ72/7wt%$Bi_2O_3$ in Fig. 4.34 and Table 4.3 revealed that the grey and white areas were mainly BNZ and $Bi_2O_3$, respectively. This supported apparently $Bi_2O_3$-based secondary phase present in the ceramics with $x$ = 7 and 10 wt%, while the sample with $x$ = 4 wt% showed a more homogeneous microstructure. XRD analysis in Fig. 4.31 confirmed well with SEM images for the ceramics with $x$ = 7 and 10 wt%, showing the presence of the secondary phases. Also, frequency distribution of the ceramics with $x$ = 4, 7 and 10 wt% show the grain size increase with broader grain size distribution. However, the mentioned grain growth mechanism was still enough to close the open pores in the ceramics, leading to higher relative density. BNZ72/4wt%$Bi_2O_3$ specimen sintered at 850°C was considered to be the representative of BNZ ceramics for further property investigation due to the fact that this sample possessed the accepted relative density and good homogeneity.

In general, for the property investigation of materials, a high-quality sample of the studied materials should be emphasized first. Therefore, based on this chapter, BNZ powder and ceramic processing were described in detail in order to obtain good sample for this novel compound. According to the above-mentioned studies, the

results revealed the optimized condition for BNZ powder and ceramics using the mixed oxide method and the conventional sintering technique, respectively. To extend knowledge about BNZ system, the specimens fabricated from the optimized condition were subsequently studied for mechanical, thermal expansion, dielectric and ferroelectric properties in the following chapter.

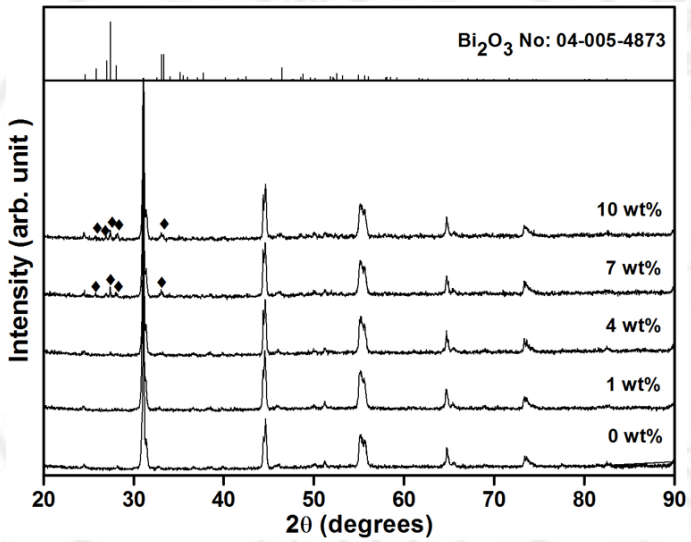


**Figure 4.31** XRD patterns of BNZ/$x$$Bi_2O_3$ ceramics sintered at 850˚C.

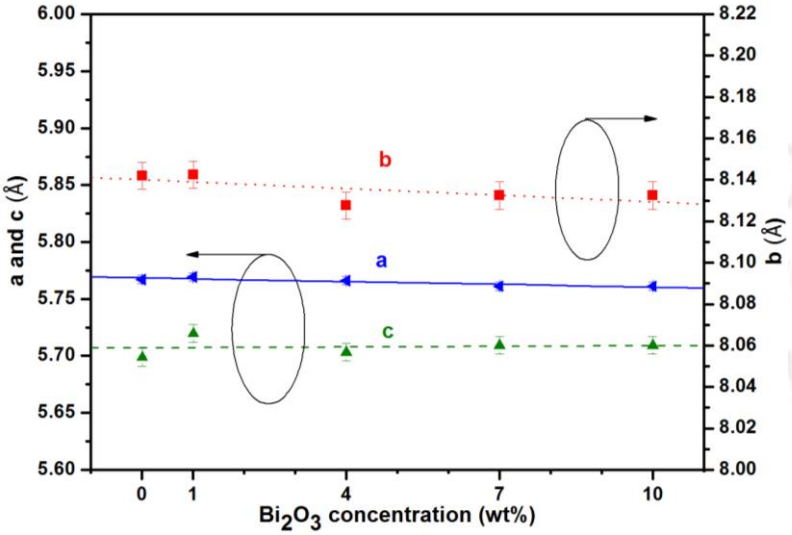


**Figure 4.32** Lattice parameters of BNZ/$x$$Bi_2O_3$ ceramics sintered at 850˚C.

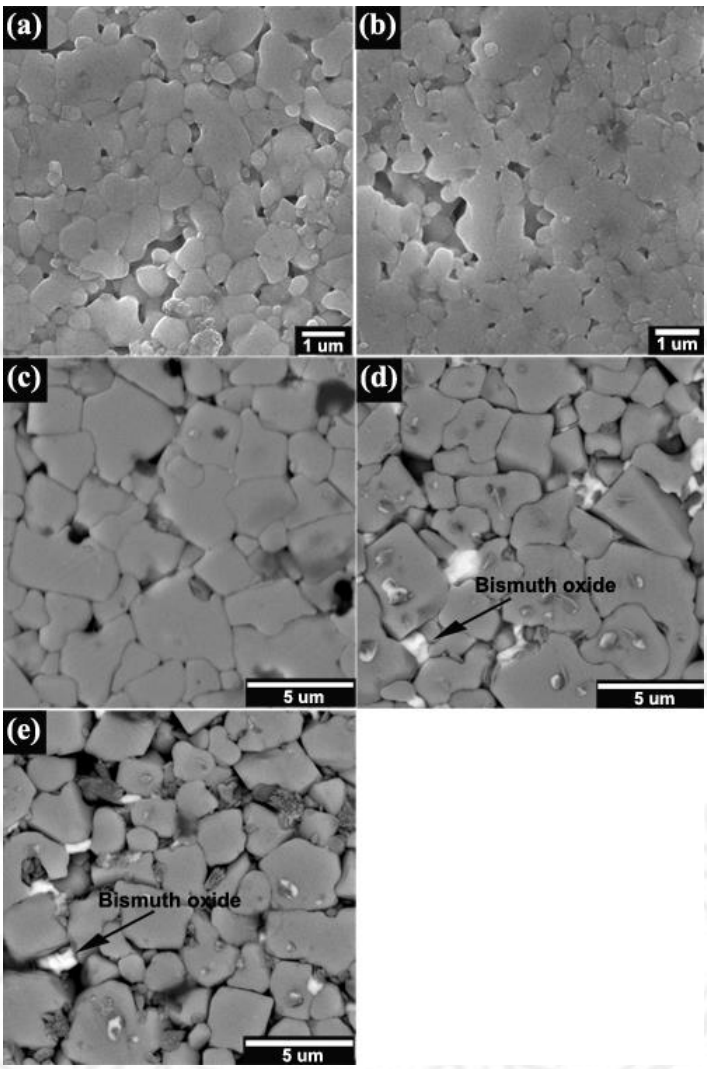


**Figure 4.33** SEM images of BNZ/$x$$Bi_2O_3$ ceramics sintered at 850˚C, where a = 0, b = 1, c = 4, d = 7 and e = 10 wt%.

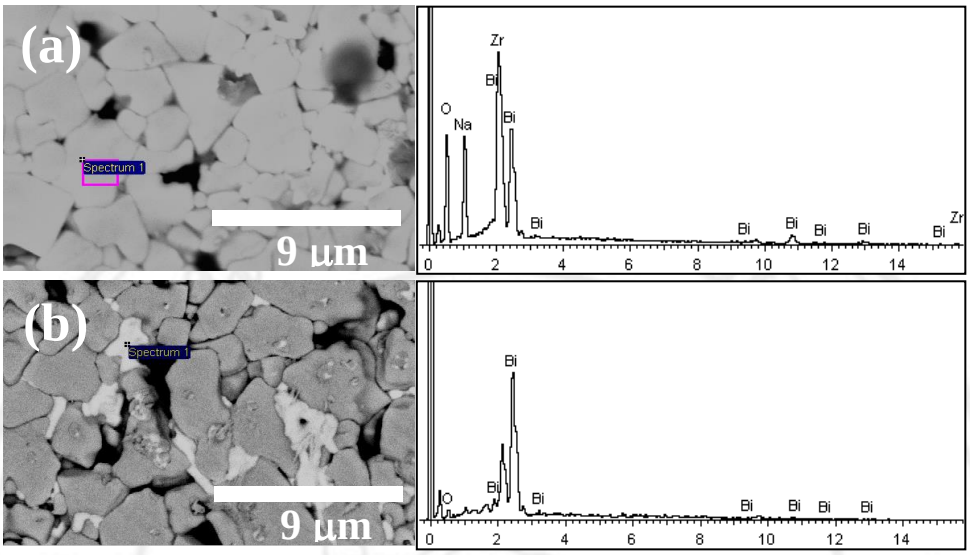


**Figure 4.34** EDX analysis of the selected areas of BNZ/7wt%$Bi_2O_3$ ceramic where a = gray area and b = white area.

**Table 4.3** Atomic amount of the selected areas of BNZ/7wt%$Bi_2O_3$ ceramic.

| Elements | Gray area Atomic (%) | White area Atomic (%) |
|---|---|---|
| Bi | 11.15 ± 1.68 | 35.45± 3.59 |
| Na | 9.19 ± 2.03 | - |
| Zr | 20.86 ± 2.45 | - |
| O | 57.80± 4.32 | 64.55 ± 3.43 |

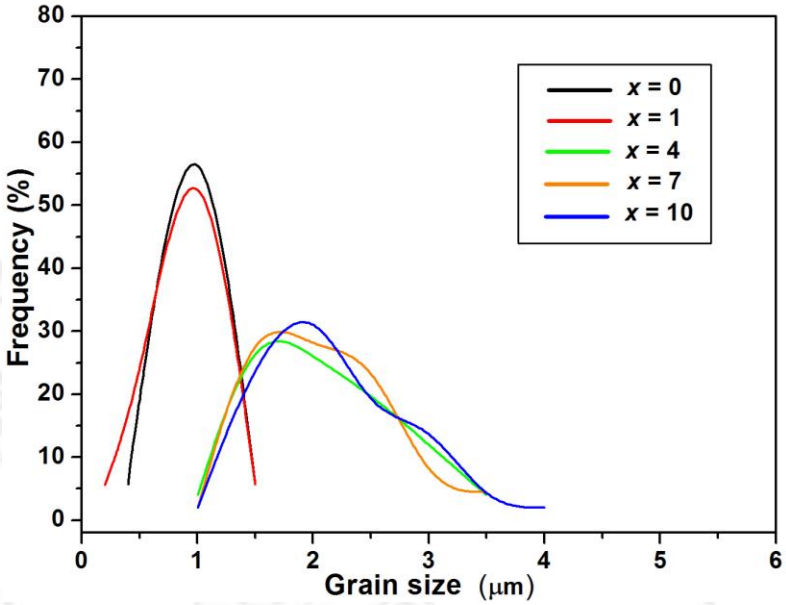


**Figure 4.35** Frequency distribution of BNZ/$Bi_2O_3$ grain sized ceramics sintered at 850°C.